

# J-shaped stress-strain diagram of collagen fibers: Frame tension of triangulated surfaces with fixed boundaries

Yu Takano and Hiroshi Koibuchi\*

*National Institute of Technology, Ibaraki College, Nakane 866, Hitachinaka, Ibaraki 312-8508, Japan*

(Received 7 July 2016; revised manuscript received 20 March 2017; published 26 April 2017)

We present Monte Carlo data of the stress-strain diagrams obtained using two different triangulated surface models. The first is the canonical surface model of Helfrich and Polyakov (HP), and the second is a Finsler geometry (FG) model. The shape of the experimentally observed stress-strain diagram is called J-shaped. Indeed, the diagram has a plateau for the small strain region and becomes linear in the relatively large strain region. Because of this highly nonlinear behavior, the J-shaped diagram is far beyond the scope of the ordinary theory of elasticity. Therefore, the mechanism behind the J-shaped diagram still remains to be clarified, although it is commonly believed that the collagen degrees of freedom play an essential role. We find that the FG modeling technique provides a coarse-grained picture for the interaction between the collagen and the bulk material. The role of the directional degrees of freedom of collagen molecules or fibers can be understood in the context of FG modeling. We also discuss the reason for why the J-shaped diagram cannot (can) be explained by the HP (FG) model.

DOI: [10.1103/PhysRevE.95.042411](https://doi.org/10.1103/PhysRevE.95.042411)

## I. INTRODUCTION

The mechanical properties of macroscopic membranes, such as human skin, have been extensively studied experimentally for a long time [1–3]. One interesting mechanical property is the stress-strain diagram. This diagram is called “J-shaped” because of its plateau (linear behavior) in the small (large) strain region [4–8]. This J-shaped curve is quite different from the curve expected from the theory of elasticity, and it is also different from the curve observed in rubber elasticity [9]. Moreover, from an engineering perspective, this nonlinear behavior attracts a considerable amount of attention for biomaterial functional technology [10,11]. For these reasons, many efforts have been devoted to understanding the origin of such a specific and unusual response to external forces. However, the mechanism still remains unclear, although it is widely accepted that the internal structure such as the collagen degrees of freedom [12–14], the notion of collagen network [15–18], and the notion of fibers [19,20] play essential roles in the J-shaped behavior.

In this paper, we use surface models for membranes, such as the Helfrich and Polyakov (HP) model [21–26] and a Finsler geometry (FG) model [27,28], to calculate the stress-strain diagram. The purpose of this study is to clarify the J-shaped behavior from the perspective of the theory of two-dimensional surfaces, which undergo thermal fluctuations. In such two-dimensional surface models, the stress  $\tau$  can be obtained as the frame tension of the surface that spans the fixed boundaries [29–31]. We will show that the J-shaped curve of  $\tau$  can be obtained in the context of the HP model. However, a linear response of  $\tau$  against the strain is also detected in an intermediate region of the bending rigidity  $\kappa$ . This linear behavior at the low strain region contradicts the existing experimental data [2–4]. In contrast, the J-shaped curve of  $\tau$  can be obtained independently of  $\kappa$  in the FG model. From this result, we confirm that the stress-strain diagrams

obtained using the FG model are consistent with the existing experimental data.

The FG model is an extension of the HP model; hence, the Hamiltonian is composed of the Gaussian bond potential  $S_1$  and the bending energy  $S_2$  [27]. Moreover, the Hamiltonian includes the sigma model Hamiltonian  $S_0$  for variable  $\sigma$ , which represents directional degrees of freedom of collagen or some internal molecular structures such as liquid crystals (LCs). This variable  $\sigma$  plays an important role in the J-shaped curve of the stress-strain diagram, just like the polymeric degrees of freedom in the aforementioned collagen network and fiber models. We also note that the variable  $\sigma$  in this paper corresponds to the one used in the FG model [28] to represent the directional degrees of freedom of LC molecules in three-dimensional (3D) liquid-crystal elastomers [32–35]. We also note that the FG model in this paper is identical to the one introduced in Ref. [36], where the surface tension and string tension of membranes are calculated on spherical and disk surfaces. In this paper, we use a cylindrical surface for calculating the diagram; thus, both the boundary conditions and the results in this paper differ from those reported in Ref. [36].

## II. MODEL

### A. Frame tension of cylindrical surface

Let us assume that an external force  $f$  is applied to a square surface, the size of which is supposed to be  $L \times H$  [Fig. 1(a)]. Let  $\tau$  be the surface tension; then, we have  $f = \tau L$ , and therefore, the accumulated surface-tension energy is given by  $F = \int_{H_0}^H f dz = \tau L(H - H_0) = \tau A_p + \text{const}$ , where  $A_p = LH$  is the surface area. This surface area  $A_p$  is the projected area of the frame, and therefore,  $A_p$  is not always identical to the real surface area  $A$  if the surface is fluctuating. Thus, the surface tension  $\tau$  is called *frame tension* if the real surface area deviates from the projected area  $A_p$  due to the surface fluctuations [30,31]. This frame tension  $\tau$  is the one that we would like to calculate in this paper. In

\*koibuchih@gmail.com

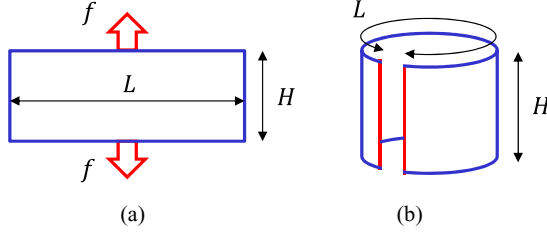


FIG. 1. (a) An external force  $f$  is applied to the square surface of the projected area  $A_p (= LH)$ ; (b) a cylindrical surface is made from the square surface by removing the vertical boundaries.

this paper, not only macroscopic membranes such as human skin but also microscopic membranes are assumed as the research targets, where the thermal fluctuations are not always negligible.

A cylindrical surface is used for calculating the frame tension  $\tau$  [Fig. 1(b)]. We use this cylindrical surface because the cylinder has no boundary except the one to which an external force is applied. A triangulated cylinder of size  $N=297$  is shown in Fig. 2(a), where the height  $H$  and the diameter  $D$  are assumed to be identical:  $H=D$ . Let  $N_1$  ( $N_2$ ) be the total number of vertices in the height (circumferential) direction; then, we have  $N=N_1 \times N_2$ ,  $H=\sqrt{3}(N_1-1)a/2$ , and  $D=N_2a/\pi$ , where  $a$  is the triangle edge length. Thus, the ratio  $N_2/N_1=\sqrt{3}\pi/2$  is independent of the size  $N$  (in the limit of  $N_1, N_2 \rightarrow \infty$ ), and all cylinders that we use in the simulations are characterized by this ratio.

### B. Finsler geometry model

In this section, we introduce a FG model, which is identical to the one introduced in Ref. [36]. The outlines of the discrete model and the corresponding continuous model are shown in this section and the Appendix A, respectively, in a self-contained manner. First, we introduce the variable  $\sigma_i \in S^2$  (unit sphere) to represent the directional degrees of freedom of liquid-crystal molecules (or collagen molecules). The Hamiltonian of the FG surface model is simply obtained by replacing the surface metric  $g_{ab}$  with a Finsler metric (see Appendix). To describe the interaction between the variables

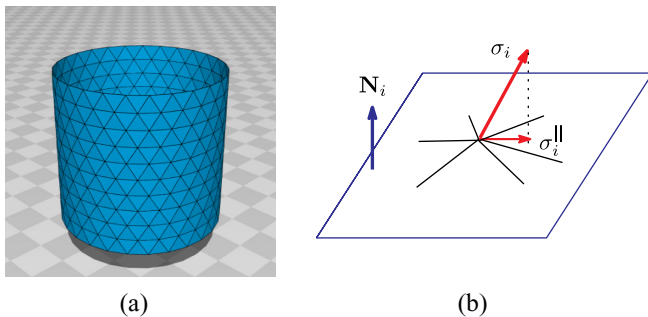


FIG. 2. (a) A cylindrical surface of size  $N=297$ , which is made of the rectangle of  $(N_1, N_2)=(11, 27)$ ; (b) a unit normal vector  $\mathbf{N}_i$  of the tangential plane at the vertex  $i$ , and the tangential component  $\sigma_i^{\parallel}$  of  $\sigma_i$ .

$\sigma$  themselves, we include the sigma model energy  $\lambda S_0$  in the Hamiltonian  $S$  with the interaction coefficient  $\lambda$  such that

$$S(\sigma, \mathbf{r}) = \lambda S_0 + S_1 + \kappa S_2 + U_B,$$

$$S_0(\sigma) = \begin{cases} -\sum_{ij} \sigma_i^{\parallel} \cdot \sigma_j^{\parallel} & \text{(polar)} \\ -(3/2) \sum_{ij} (\sigma_i^{\parallel} \cdot \sigma_j^{\parallel})^2 & \text{(nonpolar)}, \end{cases}$$

$$U_B = \sum_{i \in \text{boundary}} U_B(\mathbf{r}_i),$$

$$U_B(\mathbf{r}_i) = \begin{cases} \infty & (|z_i - H| > \delta_B \text{ or } |z_i| > \delta_B) \\ 0 & \text{(otherwise)}, \end{cases} \quad (1)$$

where  $\sigma_i^{\parallel}$  [see Fig. 2(b)] is defined as

$$\sigma_i^{\parallel} = \sigma_i - (\sigma_i \cdot \mathbf{N}_i) \mathbf{N}_i. \quad (2)$$

In  $S_0$  of Eq. (1), we assume the factor 3/2 for the nonpolar interaction, because Lebwohl-Lasher potential for LCs includes this factor, although LCs are not always included in collagen fibers [37]. In our FG model, the variable  $\sigma$  represents the direction of the collagen molecule as mentioned above. The collagen fiber is made of collagen fibrils, which are made of collagen molecules (a hierarchical structure), and therefore the fiber becomes relatively stiff [11]. In addition, the fibers are loosely connected by cross-linkers. For these reasons, the collagen fiber networks are always locally ordered. This is in sharp contrast to the case of polymers, which have not only crystalline but also randomly disordered structure. Therefore, the collagen fiber networks change from locally ordered to globally ordered states when they are expanded by external tensile forces. This coarse-grained picture of the locally ordered structure of a fiber network is expressed by the energy term  $\lambda S_0$  with finite  $\lambda$  for  $\sigma$  in our FG model. The reason why the polar interaction is also assumed for  $\sigma$  is simply to compare the results with those of a nonpolar interaction. The coefficient  $\lambda$  of  $S_0$  is fixed to  $\lambda=1$  in both polar and nonpolar interactions in the simulations. The fact that  $\lambda$  is fixed to  $\lambda=1$  is the cause of the locally ordered configuration of  $\sigma$ , although  $\lambda=1$  corresponds to the isotropic phase at least for the small strain region.

The stiffness of the fibers can be measured by  $EI$ , where  $E$  is the Young modulus and  $I$  the second moment of area. This  $EI$  is called bending rigidity, which measures the stiffness of macroscopic elastic materials. In contrast, the bending rigidity  $\kappa$  in Eq. (1) corresponds to the stiffness of microscopic membranes such as red cells. Thus,  $\kappa$  in Eq. (1) should be simply considered as a microscopic parameter that can be controlled depending on the rigidity of the fibers in consideration.

The vector  $\mathbf{N}_i$  is the unit normal vector of the surface at vertex  $i$ , and it is defined as

$$\mathbf{N}_i = \frac{\sum_{j(i)} A_{j(i)} \mathbf{n}_{j(i)}}{\left| \sum_{j(i)} A_{j(i)} \mathbf{n}_{j(i)} \right|}, \quad (3)$$

where  $A_{j(i)}$  and  $\mathbf{n}_{j(i)}$  denote the area and the unit normal vector of the triangle  $j(i)$  sharing the vertex  $i$ , respectively. Note that  $S_0$  is implicitly dependent on  $\mathbf{r}$  because  $\sigma_i^{\parallel}$  depends on the surface shape. The expressions for the Gaussian bond potential

$S_1$  and the bending energy  $S_2$  are

$$\begin{aligned} S_1 &= \frac{1}{6} \sum_{\Delta} [\gamma_{12} \ell_{12}^2 + \gamma_{23} \ell_{23}^2 + \gamma_{31} \ell_{31}^2], \\ S_2 &= \frac{1}{6} \sum_{\Delta} [\kappa_{12}(1 - \mathbf{n}_0 \cdot \mathbf{n}_1) + \kappa_{23}(1 - \mathbf{n}_0 \cdot \mathbf{n}_3) \\ &\quad + \kappa_{31}(1 - \mathbf{n}_0 \cdot \mathbf{n}_2)], \\ \gamma_{12} &= \frac{v_{12}}{v_{13}} + \frac{v_{21}}{v_{23}}, \quad \gamma_{23} = \frac{v_{23}}{v_{21}} + \frac{v_{32}}{v_{31}}, \\ \gamma_{31} &= \frac{v_{31}}{v_{32}} + \frac{v_{13}}{v_{12}}, \\ \kappa_{12} &= \frac{v_{13}}{v_{12}} + \frac{v_{23}}{v_{21}}, \quad \kappa_{23} = \frac{v_{21}}{v_{23}} + \frac{v_{31}}{v_{32}}, \\ \kappa_{31} &= \frac{v_{32}}{v_{31}} + \frac{v_{12}}{v_{13}}. \end{aligned} \quad (4)$$

The derivation of these expressions from the continuous Hamiltonians is shown in the Appendix A. The symbol  $\ell_{ij}$  is the length of bond  $ij$ , and  $v_{ij}$  is given in Eq. (A2) (see also Fig. 11 in the Appendix A).

Here we should comment on the boundary condition for the cylindrical surface. Because of the definition of  $v_{13}$  in Eq. (A2), the variable  $\sigma_1$  at vertex 1 on the boundary cannot be vertical to bond 13 on the same boundary. In fact, if  $\sigma_1 \cdot \mathbf{t}_{13} = 0$ , then we have  $v_{13} = 0$ , and therefore  $\gamma_{12} \rightarrow \infty$ . This divergence of  $\gamma_{12}$  implies that  $\sigma_1$  never be vertical to the boundary. Therefore, to remove such unphysical repulsive interaction with respect to the direction of tensile forces, we assume that the boundary vertices are able to move into the horizontal direction only slightly within small range  $\delta_B$ . This constraint for the boundary vertices is defined by the potential  $U_B$ . The small value  $\delta_B$  is given by the mean bond length, and therefore we have

$$\frac{\delta_B}{H} \left( = \frac{\text{mean bond length}}{\text{height of cylinder}} \right) \rightarrow 0 \quad (N \rightarrow \infty). \quad (5)$$

This implies that the constraint potential  $U_B$  is negligible in the limit of  $N \rightarrow \infty$ :

$$U_B \rightarrow 0 \quad (N \rightarrow \infty), \quad (6)$$

while  $\sigma$  can be vertical to the boundaries or parallel to the direction of tensile forces.

The discrete partition function  $Z$  is given by

$$\begin{aligned} Z(\lambda, \kappa; L) \\ = \sum_{\sigma} \int \prod_{i=1}^{2N_2} d\mathbf{r}_i \prod_{i=1}^{N-2N_2} d\mathbf{r}_i \exp[-S(\sigma, \mathbf{r})], \end{aligned} \quad (7)$$

where  $Z(\lambda, \kappa; L)$  denotes that  $Z$  depends on the parameters  $\lambda, \kappa$  and the height  $L$  of the cylindrical surface.  $\int \prod_{i=1}^{2N_2} d\mathbf{r}_i$  denotes the multiple  $4N_2$ -dimensional integration for the  $2N_2$  vertices on the upper and lower boundaries of the cylinder. The vertices on the boundaries are prohibited from moving in the height direction, and hence, the corresponding integration  $\int d\mathbf{r}_i$  becomes a two-dimensional integration. In contrast, the vertices on the surface, except for those on the boundaries, are not constrained by the boundaries; therefore,  $\int \prod_{i=1}^{N-2N_2} d\mathbf{r}_i$  is understood to be the  $3(N-2N_2)$ -dimensional integrations for those  $N-2N_2$  vertices.

### C. Formula for calculating stress-strain diagram

The surface position  $\mathbf{r}$  is the variable that is integrated out in the partition function  $Z$ , and for this reason,  $Z$  becomes invariant under the change of the integration variable such that  $\mathbf{r} \rightarrow \alpha \mathbf{r}$  ( $\alpha \in \mathbf{R}$ ). This property is called the scale invariance of  $Z$ , and it is used for calculating the stress-strain curve [29].

The scale invariance implies that  $Z$  should be independent of the scale parameter  $\alpha$  [38]:

$$dZ/d\alpha|_{\alpha=1} = 0. \quad (8)$$

The scaled partition function is given by

$$\begin{aligned} Z(\alpha; \alpha^{-2} A_p) \\ = \alpha^{3N-2N_2} \sum_{\sigma} \int \prod_{i=1}^{2N_2} d\mathbf{r}_i \prod_{i=1}^{N-2N_2} d\mathbf{r}_i \exp[-S(\sigma, \alpha \mathbf{r})], \\ \times S(\sigma, \alpha \mathbf{r}) = \lambda S_0 + \alpha^2 \gamma S_1 + \kappa S_2, \end{aligned} \quad (9)$$

where  $\alpha^{-2} A_p$  in  $Z(\alpha; \alpha^{-2} A_p)$  denotes the dependence of  $Z$  on  $\alpha$  arising from the fact that the projected area  $A_p$  is fixed. This dependence of  $Z$  on  $\alpha$  implies that  $Z$  can be considered to be a two-component function. Thus, from Eq. (8), we obtain  $dZ/d\alpha = \partial Z/\partial\alpha + [\partial Z/\partial(\alpha^{-2} A_p)][\partial(\alpha^{-2} A_p)/\partial\alpha] = 0$ . Dividing Eq. (8) by  $Z$  and using  $\partial(\alpha^{-2} A_p)/\partial\alpha = -2A_p \alpha^{-3}$ , we have

$$3N - 2N_2 - 2\gamma \langle S_1 \rangle - 2 \frac{A_p}{Z} \frac{\partial Z}{\partial A_p} = 0. \quad (10)$$

The mean value of the Gaussian energy  $\langle S_1 \rangle$  on the left-hand side is obtained by Monte Carlo (MC) simulations. However, the problem here is how to evaluate the final term  $(1/Z) \partial Z/\partial A_p$ . To calculate this term, we assume that the free energy  $F$  is given by

$$F = \tau \int_{A_0}^{A_p} dA = \tau(A_p - A_0), \quad (11)$$

where  $\tau$  is the frame tension as mentioned above. Because the corresponding partition function is given by  $Z = \exp(-F)$ , we finally obtain  $\tau = (2\gamma \langle S_1 \rangle - 3N + 2N_2)/(2A_p)$ .

The problem now is how to obtain the projected area  $A_p$  in this  $\tau$ . Let  $D$  and  $H$  be the diameter and the height of the cylinder, respectively. Then, it is natural to define  $A_p$  as  $A_p = \pi DH$  if  $D$  is uniform in the sense that  $D$  is independent of the height position  $h$  of the cylinder. Note that  $D$  corresponds to  $L/\pi$  for the cylinder, such as the one in Fig. 1(b). However, the diameter  $D$  is expected to generally depend on  $h$  because the cylinder is not a three-dimensional one but rather a two-dimensional surface, and therefore,  $D$  at the height position  $h = H/2$  may be different from  $D$  at  $h \simeq H$  or  $h \simeq 0$ , for example. For this reason, we use the diameter  $D_0 (= H_0)$  of the initial surface, which is used for the simulations of  $\tau = 0$ . Thus, the formula for  $\tau$  is given by

$$\begin{aligned} \tau &= (2\gamma \langle S_1 \rangle - 3N + 2N_2)/(2A_p), \\ A_p &= \pi D_0 H \quad (\gamma = 1). \end{aligned} \quad (12)$$

### D. Monte Carlo technique

The multiple-dimensional integrations in  $Z$  are simulated using the standard Metropolis Monte Carlo technique [39,40].



The update of the vertex position  $\mathbf{r}$  is performed with the probability  $\text{Min}[1, \exp(-\delta S)]$ , where  $\delta S = S(\text{new}) - S(\text{old})$  with the new position  $\mathbf{r}' = \mathbf{r} + \delta \mathbf{r}$ . The small change  $\delta \mathbf{r}$  is randomly distributed in a small sphere (or circle) of radius  $R_\delta$ , which is fixed to keep an approximately 50% acceptance rate of  $\mathbf{r}'$ . The vertices on the boundaries are allowed to move only in the horizontal plane ( $\mathbf{R}^2$ ), whereas the other vertices move in the three-dimensional space  $\mathbf{R}^3$ . The variable  $\sigma$  is updated such that the new variable  $\sigma' (\in S^2)$  is completely independent of the old  $\sigma$ . One Monte Carlo sweep (MCS) consists of  $N$  consecutive updates for  $\mathbf{r}$  and  $N$  consecutive updates for  $\sigma$ . After a sufficiently large number of MCSs, measurements of physical quantities are performed every 1000 MCSs. All the simulations in this paper are performed on lattices of size  $N = 10584$ .

The initial height  $H_0 (= D_0)$  for the frame tension  $\tau$  in Eq. (12) is determined such that the equilibrium configurations satisfy  $\tau = 0$ . From this definition of  $D_0$  and that of  $A_p$ , the frame tension  $\tau$  in Eq. (12) is considered to be the nominal stress in the sense that  $\tau$  is independent of  $\pi(D)$ , the real length of the circumference of the cylinder. To be more precise,  $\pi(D)$  can be identified using the real length of the circumference of the cylinder only when the cylinder is sufficiently smooth and has no surface fluctuations. In the case of the 3D liquid-crystal elastomer (LCE), the nominal stress is calculated with a constant sectional area, which is independent of the height of the cylinder [28]. In contrast, the projected area  $A_p$  for  $\tau$  in Eq. (12) is proportional to the height  $H$  of the cylinder. Note that the diameter  $D_0 (= H_0)$  is not always identical to  $\langle D \rangle$  (the symbol  $\langle \rangle$  is not used henceforth, for simplicity); however, the deviation between  $D_0$  and  $D$  is expected to be small because the cylinder is constructed such that the diameter equals the height for  $\tau = 0$ .

### III. RESULTS

#### A. Snapshots

First, we show snapshots of surfaces of the nonpolar model in Fig. 3. From the snapshots, we confirm that the variable  $\sigma$  is locally ordered when  $H/H_0 = 1$  for  $\kappa = 1$ , while it is globally ordered along the vertical direction when  $H/H_0 = 1.4$  [Figs. 3(a) and 3(b)]. The reason why  $\sigma$  is locally ordered is because the coefficient  $\lambda$  of  $S_0$  is fixed to  $\lambda = 1$ . For the case  $\kappa = 3$ , we can also see almost the same ordering of  $\sigma$  on the surfaces [Figs. 3(c) and 3(d)].

#### B. Canonical model

In this section, we present the results of the HP (or canonical) model and discuss why the canonical model is insufficient for explaining the existing experimental data of the J-shaped stress and strain diagram [1–4]. The canonical model is defined as

$$Z(\kappa; L) = \int \prod_{i=1}^{2N_2} d\mathbf{r}_i \prod_{i=1}^{N-2N_2} d\mathbf{r}_i \exp[-S(\mathbf{r})],$$

$$S(\mathbf{r}) = S_{-1} + \kappa S_3 \quad (\text{canonical}),$$

$$S_{-1} = \sum_{ij} \ell_{ij}^2, \quad S_3 = \sum_{ij} (1 - \mathbf{n}_i \cdot \mathbf{n}_j), \quad (13)$$

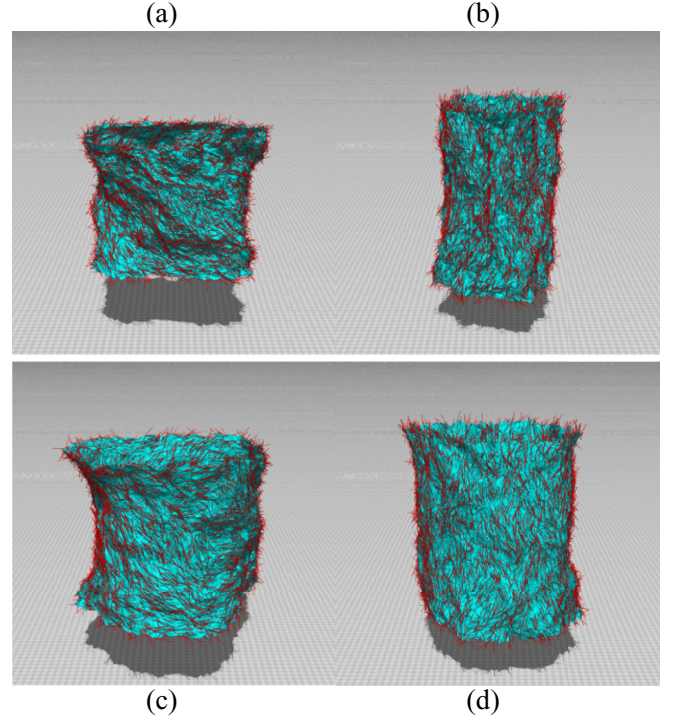


FIG. 3. Snapshots of surfaces of the nonpolar model for  $\kappa = 1$  with (a)  $H/H_0 = 1$  and (b)  $H/H_0 = 1.4$ , and for  $\kappa = 3$  with (c)  $H/H_0 = 1$  and (d)  $H/H_0 = 1.24$ . The short lines (or burs) on the surfaces represent the variable  $\sigma$ .  $N = 10584$  and  $\lambda = 1$ .

where  $\ell_{ij}^2 = (\mathbf{r}_i - \mathbf{r}_j)^2$  is the bond-length squares [23,26,29]. In Eq. (13), we use the symbols  $S_{-1}$  and  $S_3$  for the canonical Gaussian energy and the bending energy, respectively, to distinguish them from  $S_1$  and  $S_2$  in Eq. (1) for the FG model. Note that these  $S_{-1}$  and  $S_3$  are not assumed as Hamiltonians in the FG model; however, these quantities can be obtained (or calculated) from the surface configurations of the FG model.

As shown in Fig. 4(a),  $\tau$  is linear with respect to  $H/H_0$  for  $\kappa = 1.5$  and  $\kappa = 1$ . This figure also shows that the shape of  $\tau$  changes from linear to J-shaped when  $\kappa$  increases from  $\kappa = 1.5$  to  $\kappa = 3$ ,  $\kappa = 5$ , and  $\kappa = 7$ . It is also observed that  $\tau$  becomes J-shaped when  $\kappa$  decreases from  $\kappa = 1.5$  to  $\kappa = 0.75$ . To evaluate the surface smoothness, we plot the bending energy  $S_3/N_B$  in Fig. 4(c), where  $N_B$  is the total number of bonds excluding the bonds on the boundaries on which  $S_3$  is not defined. We find that the plateau of  $\tau$  can be observed on the relatively smooth surfaces of  $S_3/N_B \leq 0.07$  and on the relatively wrinkled surfaces of  $S_3/N_B \geq 0.4$ . On the surfaces of  $S_3/N_B \simeq 0.2$ ,  $\tau$  becomes linear with respect to  $H/H_0$ . The mean triangle area  $A$ , which is defined as

$$A = (1/N_T) \sum_{\Delta} A_{\Delta}, \quad (14)$$

is also J-shaped if the corresponding  $\tau$  is J-shaped [Fig. 4(d)], where  $N_T$  is the total number of triangles. Only for  $\kappa = 1.5$  is the mean triangle area  $A$  almost linear. The J-shaped behavior of  $A$  implies that the real surface area remains unchanged for the small  $H/H_0 (> 1)$  region, whereas the projected area  $A_p$  always changes linearly with respect to  $H/H_0$ .

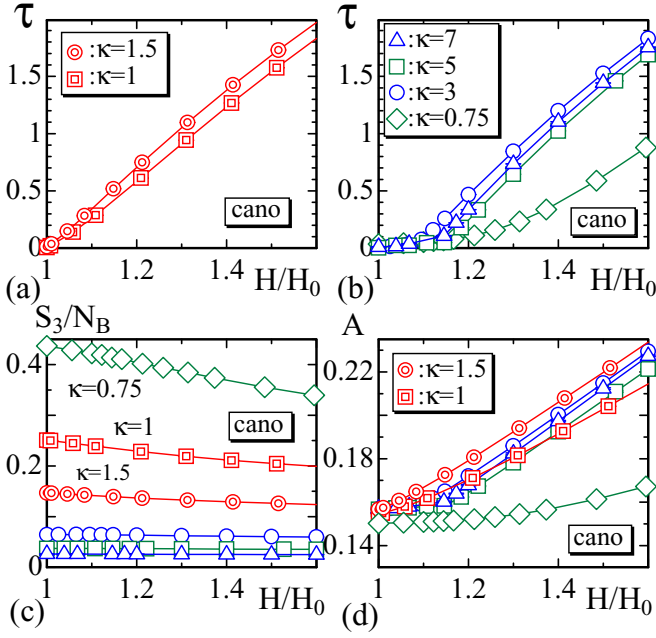


FIG. 4. The stress  $\tau$  vs strain  $H/H_0$  of the canonical model for (a)  $\kappa=1, \kappa=1.5$  and (b)  $3 \leq \kappa \leq 7, \kappa=0.75$ ; (c) the bending energy  $S_3/N_B$  vs  $H/H_0$ ; and (d) the mean triangle area  $A$  vs  $H/H_0$ , where  $S_3$  is defined in Eq. (13).  $N = 10584$ .

Thus, we observe that the behavior of  $\tau$  for  $\kappa \simeq 0.75$  and  $3 \leq \kappa \leq 7$  appears J-shaped, and hence, this observation indicates that the J-shaped diagram can be understood within the context of the canonical model. However, the problem is the linear behavior of  $\tau$  observed in the intermediate region  $\kappa \simeq 1.5$ . These results also imply that  $\tau$  has J-shaped behavior at low and high temperatures, whereas it has a linear behavior at intermediate temperatures because  $\kappa$  has units of  $k_B T$ . To summarize these results, the linear  $\tau$  at  $\kappa \simeq 1.5$  conflicts with the existing experimental results [1–4], at least in the context of the canonical model.

The problem is why linear behavior is observed only at the intermediate region of  $\kappa$ . We first note that the linear behavior of  $\tau$  for the large  $H/H_0$  region is easy to understand. For the large  $H/H_0$  region, the surface area is increased to a sufficiently large value, while the bending energy  $S_3$  is negligible compared with  $S_{-1}$ , which has units of length squares; hence, the energy supplied by the external force is accumulated only in  $S_{-1}$ . The interesting region of  $H/H_0$  is close to  $H/H_0 = 1$ , where the surface can fluctuate if  $\kappa$  is not very large. For the small  $\kappa$  region, the surface is sufficiently wrinkled, and therefore, the surface height  $H$  is increased without changing the bond length for  $H/H_0$  close to  $H/H_0 = 1$ . On such rough surfaces, the long-wavelength mode of surface fluctuations is not expected. This means that the persistence length  $\xi$  is relatively short, and hence, the external force at one of the two boundaries has no influence on the other boundary. However, when  $\kappa$  is increased to  $\kappa \simeq 1.5$ , the surface becomes relatively smooth such that the long-wavelength modes (or long-range correlations of surface fluctuations, such as surface normals) are expected to appear on the surface, and therefore, the external force applied on the boundary influences the

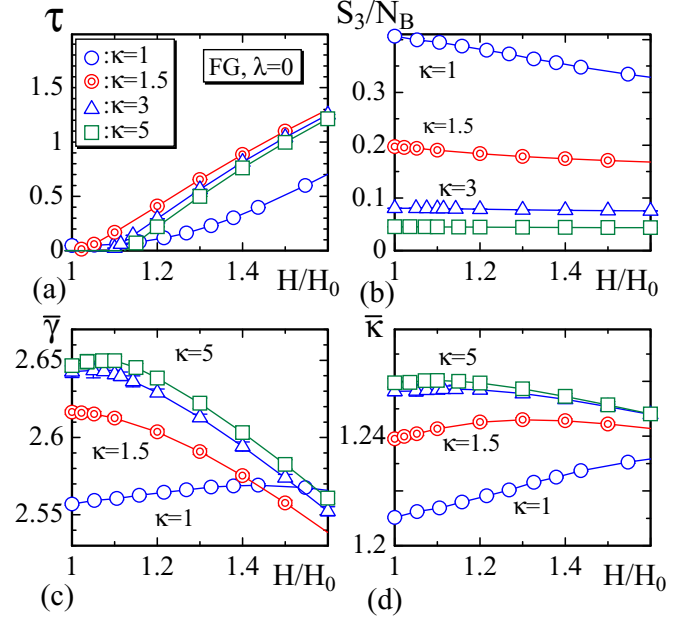


FIG. 5. MC data of the FG model for  $\lambda=0$ : (a)  $\tau$  vs  $H/H_0$ , (b)  $S_3/N_B$  vs  $H/H_0$ , (c)  $\bar{\gamma}$  vs  $H/H_0$ , and (d)  $\bar{\kappa}$  vs  $H/H_0$ .  $N = 10584$ .

entire surface such that  $S_{-1}$  can be increased even for the small  $H/H_0$  region. This is a reason for why no plateau is observed in  $\tau$  in the intermediate region of  $\kappa$ . For the large  $\kappa$  region, such as  $\kappa \simeq 5$ , the surface is further smoothed, and the surface fluctuation is suppressed. On these relatively smooth surfaces with small surface fluctuations, the boundary effect is not mediated in the form of surface fluctuation modes for the small  $H/H_0$  region, and this makes a plateau in  $\tau$ .

Thus, the linear behavior of  $\tau$  for the intermediate region of  $\kappa$  is typical of the two-dimensional fluctuating surfaces; however, this linear behavior is unsatisfactory from the perspective of the experimental fact that  $\tau$  is J-shaped in biological membranes [1–4]. The main reason for this is that the surface fluctuations are expected in the canonical surface model, while they are suppressed in the macroscopic membranes such as skins and collagen fiber networks. We have to conclude that the canonical surface model is insufficient for explaining the J-shaped stress-strain diagram of macroscopic membranes.

### C. FG model for $\lambda = 0$

In this section, we evaluate the equivalence between the canonical model and the FG model for  $\lambda=0$ . When  $\lambda$  is zero in the FG model, the variable  $\sigma$  becomes random, and hence, no anisotropy is expected on the surface [27,28]. Indeed, the FG model is an extension of the canonical HP model in the sense that the outputs of the FG model for  $\lambda=0$  are consistent with those of the canonical model.

Figure 5(a) shows  $\tau$  vs  $H/H_0$  of the FG model for  $\lambda=0$  with several different values of  $\kappa$ . As shown in this figure,  $\tau$  changes linearly against  $H/H_0$  for  $\kappa=1.5$ , and  $\tau$  is J-shaped for  $\kappa=5, \kappa=3$ , and  $\kappa=1$ . From these results, it is clear that the dependence of  $\tau$  on  $H/H_0$  of the FG model for  $\lambda=0$  is consistent with that of the canonical model. Indeed, we

find from  $S_3/N_B$  shown in Fig. 5(b) that the stress  $\tau$  for the surfaces of  $S_3/N_B \simeq 0.2$  ( $S_3/N_B \leq 0.07$  and  $S_3/N_B \geq 0.35$ ) behaves linearly (has a plateau) with respect to  $H/H_0$ . This result is almost consistent with the results of the canonical model shown in Figs. 4(a)–4(c).

Note that the role of  $\kappa$  in the canonical model is not always the same as that in the FG model. Indeed,  $\kappa\kappa_{ij}$  plays the role of the bending rigidity in the FG model, whereas the constant  $\kappa$  is the bending rigidity in the canonical model. Moreover, the surface-tension coefficient  $\gamma$  is fixed to  $\gamma = 1$  in the canonical model, whereas in the FG model,  $\gamma_{ij}$  plays the role of the surface-tension coefficient. For these reasons, to clarify the relation between the coefficients in the canonical model and those in the FG model, we calculate the mean values of  $\gamma_{ij}$  and  $\kappa_{ij}$  such that

$$\begin{aligned}\bar{\gamma} &= \frac{\sum_{ij} \gamma_{ij} \ell_{ij}^2}{\sum_{ij} \ell_{ij}^2} = \frac{3S_1}{S_{-1}}, \\ \bar{\kappa} &= \frac{\sum_{ij} \kappa_{ij} (1 - \mathbf{n}_i \cdot \mathbf{n}_j)}{\sum_{ij} (1 - \mathbf{n}_i \cdot \mathbf{n}_j)} = \frac{3S_2}{S_3}.\end{aligned}\quad (15)$$

The reason for multiplying  $S_1$  and  $S_2$  by a factor of 3 in Eq. (15) is as follows. The sum of triangles  $\sum_{\Delta}$  in  $S_1$  and  $S_2$  in Eq. (4) can be replaced by the sum of bonds  $2\sum_{ij}$  because every term  $\ell_{ij}^2$  or  $1 - \mathbf{n}_i \cdot \mathbf{n}_j$  is summed over twice in the sum  $\sum_{\Delta}$ . From this factor 2, the factor 1/6 in  $S_1$ , and the expression of  $S_2$  in Eq. (4), we include the factor 3 in  $\bar{\gamma}$  and  $\bar{\kappa}$  in Eq. (15).

We observe that the dependence of  $\bar{\gamma}$  on  $H/H_0$  in Fig. 5(c) appears similar to that of  $\tau$  in Fig. 5(a). Indeed, both  $\bar{\gamma}$  and  $\tau$  have a plateau (linear behavior) for  $\kappa=5$ ,  $\kappa=3$ , and  $\kappa=1$  ( $\kappa=1.5$ ). We also observe that the value of  $\bar{\gamma}$  is in the range  $2 \leq \bar{\gamma} \leq 2.8$ , and it is larger than that of  $\gamma (=1)$  of the canonical model. However,  $\bar{\gamma}$  is included in  $S_1 (= \bar{\gamma} S_{-1})$ , and therefore, we expect that this difference between  $\bar{\gamma}$  and  $\gamma (=1)$  does not make any difference between the stresses  $\tau$  of the canonical and FG models. Indeed,  $\tau$  in Fig. 5(a) for each  $\kappa$  is almost comparable to (or slightly smaller than)  $\tau$  in Figs. 4(a) and 4(b) of the canonical model.

Using the  $\bar{\gamma}, \bar{\kappa}$  in Eq. (15) and the Hamiltonians  $S_{-1}, S_3$  in Eq. (13), we have the effective Hamiltonian for the FG model such that  $S_{\text{eff}} = \bar{\gamma} S_{-1} + \kappa \bar{\kappa} S_3$ , which can also be written as  $S_{\text{eff}} = \bar{\gamma} [S_{-1} + \kappa (\bar{\kappa}/\bar{\gamma}) S_3]$ . In these expressions of  $S_{\text{eff}}$ , the multiplicative factor 3 is dropped for simplicity. Furthermore, because the factor  $\bar{\gamma}$  in  $S_{\text{eff}}$  can be dropped due to the scale invariance of  $Z$ , we finally have  $\tilde{S}_{\text{eff}} = S_{-1} + \kappa (\bar{\kappa}/\bar{\gamma}) S_3$ .

From this  $\tilde{S}_{\text{eff}}$ , the differences between  $S_3/N_B$  of the canonical and FG models are understood. As shown in Fig. 5(d),  $\bar{\kappa}$  is slightly larger than 1;  $\bar{\kappa} > 1$ . However,  $\bar{\kappa}$  is not included in  $S_3$ , which is shown in Fig. 5(b) [ $\bar{\kappa}$  is included only in  $S_2 (= \bar{\kappa} S_3)$ ] in contrast to the case of  $\bar{\gamma}$ , which is included in  $S_1$ . For this reason,  $S_3/N_B$  of the FG model is expected to be smaller than that of the canonical model. However, the results are opposite;  $S_3/N_B$  of the FG model is slightly larger than that of the canonical model. This result can be understood from the effective Hamiltonian  $\tilde{S}_{\text{eff}} = S_{-1} + \kappa (\bar{\kappa}/\bar{\gamma}) S_3$  described above. Indeed, the fact that  $\bar{\kappa}/\bar{\gamma} < 1$  makes  $S_3$  larger. In other words, the effective bending rigidity of the FG model for  $\lambda=0$  corresponds to the slightly smaller  $\kappa$  of the canonical model for the same value of  $S_3/N_B$ . This result is consistent with the

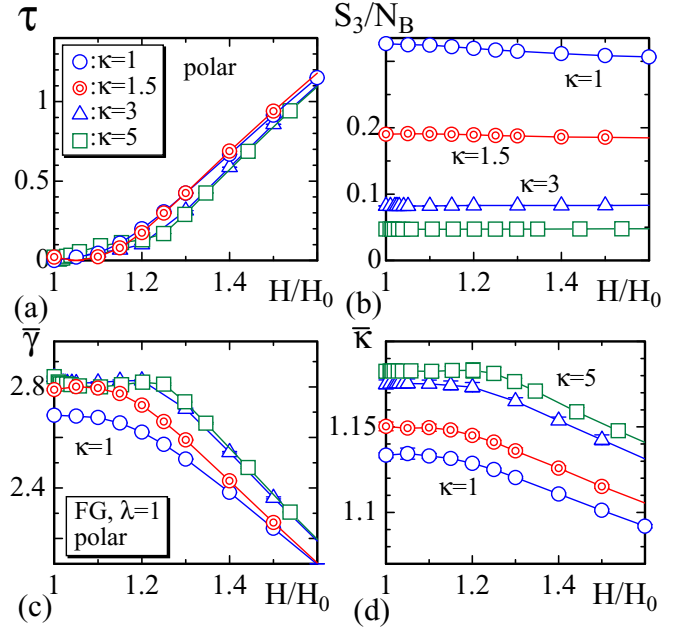


FIG. 6. MC data of the polar FG model for  $\lambda=1$ : (a)  $\tau$  vs  $H/H_0$ , (b)  $S_3/N_B$  vs  $H/H_0$ , (c)  $\bar{\gamma}$  vs  $H/H_0$ , and (d)  $\bar{\kappa}$  vs  $H/H_0$ .  $N = 10584$ .

forementioned result that  $\tau$  of the canonical model for  $\kappa=1$  is linear, whereas  $\tau$  of the FG model for  $\kappa=1$  has a plateau.

#### D. FG model for $\lambda \neq 0$

Now we turn to the nontrivial cases corresponding to  $\lambda \neq 0$ , and we will show that the results, obtained in the entire range of  $\kappa$  including the large  $\kappa$  region, are consistent with the existing J-shaped diagram. First, in Fig. 6, we present the results of the polar FG model, where  $\lambda$  is fixed as  $\lambda=1$ . The stress  $\tau$  vs  $H/H_0$  in Fig. 6(a) is found to be J-shaped for  $\kappa=1$ ,  $\kappa=1.5$ ,  $\kappa=3$ , and  $\kappa=5$ . The result for  $\kappa=1.5$  in Fig. 6(a) is new and nontrivial. Indeed, the corresponding  $S_3/N_B$  has values such that  $S_3/N_B \simeq 0.2$ , which corresponds to those for  $1.0 \leq \kappa \leq 1.5$  of the canonical model in Figs. 4(a) and 4(b), where  $\tau$  behaves linearly against  $H/H_0$ . Note that  $\tau$  for  $\kappa \neq 1.5$  is not always specific to the FG model because the corresponding  $\tau$  also has a plateau structure just like in the canonical model. The parameters  $\bar{\gamma}$  and  $\bar{\kappa}$  also have a plateau in the region of  $H/H_0$ , where  $\tau$  has the plateau.

The question is, why is there no linear behavior of  $\tau$  observed in the FG model? One possible answer is that the effective one-dimensional correlation introduced by the variable  $\sigma$  changes the property of two-dimensional surface fluctuations such that the long-range force is suppressed in the region of  $H/H_0$  close to  $H/H_0=1$ . The variable  $\sigma$  aligns along the  $z$  direction in which the cylindrical surface is expanded, and therefore, the one-dimensional correlation along this direction is expected for a relatively large region of  $\lambda$ , such as  $\lambda \geq 1$ . Indeed, it is easy to understand from  $S_1$  in Eq. (A5) that a bond length becomes large (small) if  $\sigma$  aligns parallel (vertical) to this bond. Therefore, it is natural that the surface fluctuations expected in the FG model for the large  $\lambda$  region are different from those expected in the canonical model. This phenomenon in which the long-range force is suppressed is quite analogous to the one



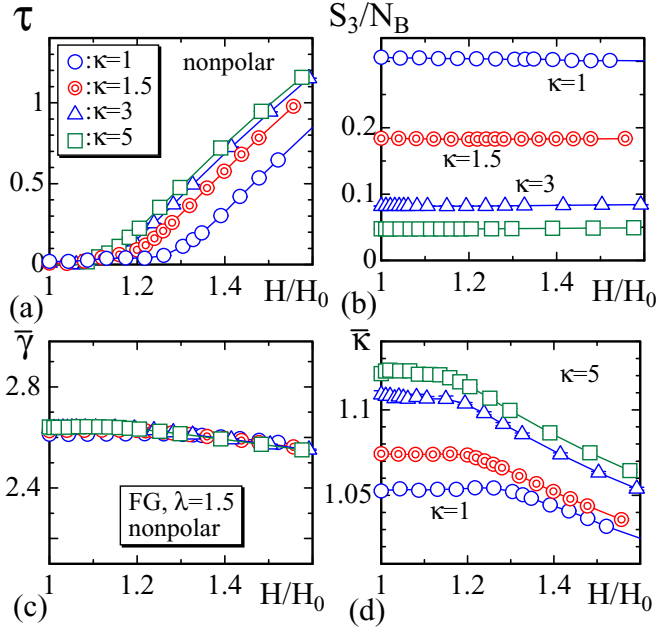


FIG. 7. MC data of the nonpolar FG model for  $\lambda=1$ : (a)  $\tau$  vs  $H/H_0$ , (b)  $S_3/N_B$  vs  $H/H_0$ , (c)  $\bar{\gamma}$  vs  $H/H_0$ , and (d)  $\bar{\kappa}$  vs  $H/H_0$ .  $N=10584$ .

reported in Ref. [41], where an  $XY$  model energy suppresses the crumpling transition on spherical surfaces, although the interaction between  $\sigma$  and the surface of the  $XY$  model in [41] is different from that of the FG model in this paper.

The results of the nonpolar FG model are presented in Fig. 7, where  $\lambda$  is fixed to  $\lambda=1.5$ . These data are consistent with those of the polar model in the region of  $\kappa$  such as  $1 \leq \kappa \leq 5$ . For all values of  $\kappa$  assumed,  $\tau$  has the J-shaped structure.

The mean triangle area  $A$  and the order parameter  $M$  for the variable  $\sigma$  defined by

$$M = \begin{cases} \sigma & (\text{polar}) \\ (3/2)[\sigma_z^2 - (1/3)] & (\text{nonpolar}) \end{cases} \quad (16)$$

are plotted in Figs. 8(a)–8(d). In Eq. (16),  $\sigma$  for the polar case is given by  $\sigma = |\sum_i \sigma_i|/N$ . A plateau can also be detected in  $A$ , like that in  $\tau$ , in both the polar and nonpolar models, and the range  $H/H_0$  of the plateau for  $A$  is almost identical to that for  $\tau$ . The area  $A$  corresponds to the real surface area; hence, it is considerably different from the projected area  $A_p$ , which is proportional to  $H/H_0$ . This difference between  $A$  and  $A_p$  implies that the radius of the cylinder shrinks in its plateau region. In fact, it is easy to understand that  $A$  has no plateau if the cylinder radius remains unreduced.

The order parameter changes such that  $M \rightarrow 0$  ( $M \rightarrow 1$ ) for  $H/H_0 \rightarrow 1$  ( $H/H_0 \rightarrow \infty$ ) in Figs. 8(b) and 8(d). This result indicates that the origin of the J-shaped curve is the structural change of  $\sigma$ . Indeed,  $M$  varies rapidly in the plateau region in both the polar and nonpolar models. The plateau of  $\tau$  is observed in the range  $1 \leq H/H_0 \leq 1.2$  ( $1 \leq H/H_0 \leq 1.3$ ) for the polar (nonpolar) model.

The eigenvalues  $\Sigma$  of the tensor order parameter defined by

$$Q_{\mu\nu} = 3(\langle \sigma_\mu \sigma_\nu \rangle - \delta_{\mu\nu}/3) \quad (17)$$

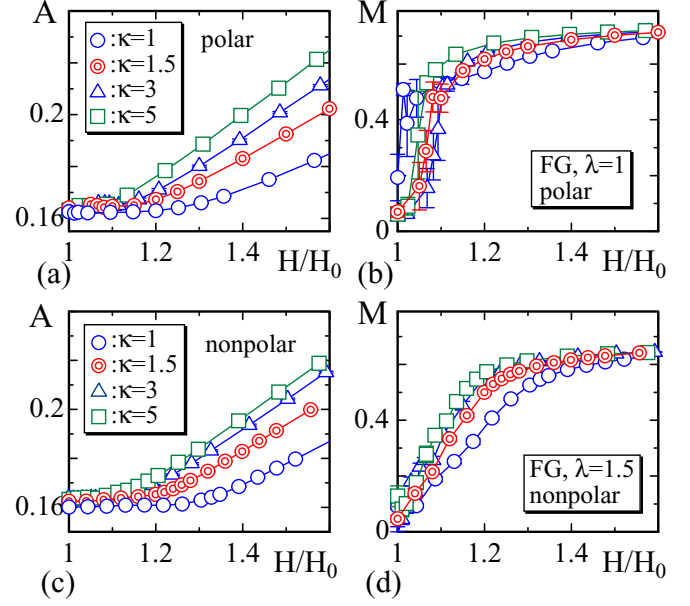


FIG. 8. (a) Tangential component  $v_{ij}$  of  $\sigma_i$  along the direction  $\mathbf{t}_{ij}$  on the triangle 123; (b) a unit normal vector  $\mathbf{N}_i$  of the tangential plane at the vertex  $i$ , and the tangential component  $\sigma_i^{\parallel}$  of  $\sigma_i$ .

are plotted in Fig. 9 for the nonpolar model. The largest eigenvalue  $\Sigma_1$  becomes  $\Sigma_1 \rightarrow 1$ , and the other two eigenvalues  $\Sigma_2$  and  $\Sigma_3$  are expected to be  $\Sigma_{2,3} \rightarrow -0.5$  if  $\sigma$  is completely ordered. We confirm also from Figs. 9(a) and 9(b) that the variable  $\sigma$  becomes ordered if  $H$  is enlarged. The behavior of ordering of  $\sigma$  is exactly consistent to that of  $M$  in Fig. 8(d). The large fluctuations of  $\Sigma_i$  in the small region of  $H/H_0$  for  $\kappa=3$  indicate that the directional change of  $\sigma$  is abrupt with respect to  $H$ .

Finally in this section, we comment on the reasons for why the bending rigidities of  $\kappa \rightarrow 0$  and  $\kappa \rightarrow \infty$  are not assumed in the calculations. First, the curves of  $\tau$  vs  $H/H_0$  are obtained under the assumption that the surface remains cylindrical in shape. However, the surface shape deviates from cylindrical and becomes very thin for the small  $\kappa$  region, such as  $\kappa=0.5$ , and collapses into stringlike configurations if  $\kappa$  is reduced to  $\kappa=0.4$ . In such a very thin surface, the surface area becomes far different from the projected area. Moreover, for these highly

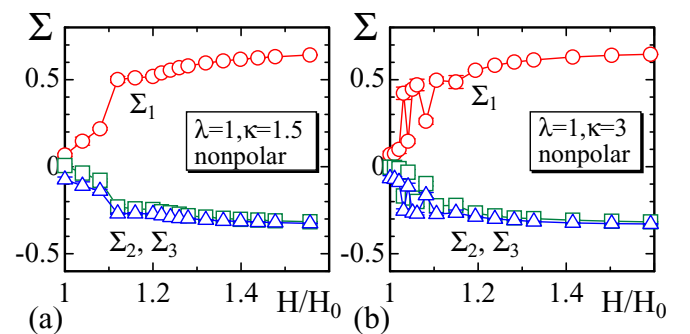


FIG. 9. Eigenvalues  $\Sigma_i$  ( $i=1,2,3$ ) of the tensor order parameter  $Q_{\mu\nu}$  in Eq. (17) of the nonpolar model for (a)  $\kappa=1.5$  and (b)  $\kappa=3$ , under  $\lambda=1$ .

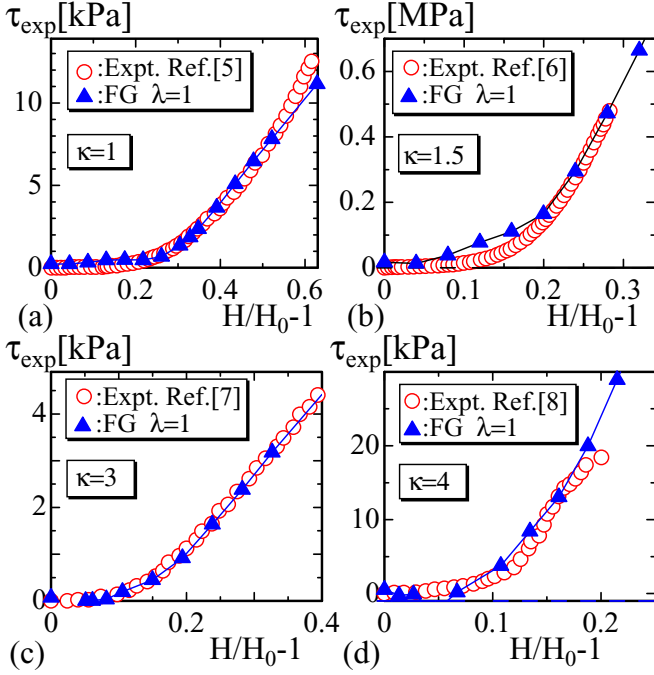


FIG. 10. The nominal stress vs strain ( $\circ$ ) of (a) blood vessel [5], (b) rat muscle [6], (c) collagen fibers [7], and (d) collagen hydrogels [8]. The solid triangle denotes the simulation data  $\tau_{\text{sim}}$  of Eq. (18) for the nonpolar interaction.

wrinkled surfaces,  $\tau$  appears to always be positive even for small  $H_0$ . This is actually expected because the surface shrinks to a small sphere for sufficiently small  $\kappa$ . For these reasons, we assume a relatively large bending rigidity ( $\kappa \geq 0.75$ ) such that the cylindrical surface shape is maintained in the range  $1 \leq H/H_0 \leq 2$ . In contrast, for the region of large  $\kappa$ , which is denoted by  $\kappa \rightarrow \infty$ ,  $S_2$  is expected to be zero, and therefore, the surface shape can be changed only in its tangential direction. In this case, only  $S_{-1}$  changes as  $H/H_0$  increases, and there is no reason for  $\tau$  to behave nonlinearly with respect to  $H/H_0$ . However, in the case that  $S_2$  is not always exactly zero, where the surface is expected to undergo buckling, we also expect a nonlinear behavior in  $\tau$ . However, in these large regions of  $\kappa$ , the model surface will be far from biological membranes.

### E. Comparison with experimental data

In this section, we show that the simulation data can be compared to the experimental stress-strain data of biological materials such as blood vessel, rat muscle, collagen fibers, and collagen hydrogels [5–8] [see Figs. 10(a)–10(d)]. First, we should comment on the unit of  $\tau$  in Eq. (12) assumed for the simulations in more detail. In the simulations, the inverse temperature  $\beta (= 1/k_B T)$  is fixed to  $\beta = 1$  ( $\Leftrightarrow k_B T = 1$ ), and under this unit the triangle edge length  $a$  is fixed to  $a = 1$ . This  $a$  corresponds to the lattice spacing in the lattice field theory language [42] and is suitably fixed such that the simulation data can be compared to the experimental data. However, the physical unit of  $\tau$  is given by [N/m], which is different from the experimental one [Pa] for stresses of macroscopic objects. For this reason, we obtain  $\tau_{\text{sim}}$  dividing the simulation data  $\tau$

TABLE I. The lattice spacing  $a$  corresponding to the stress-strain diagrams shown in Figs. 10(a)–10(d).

Fig. 10	(a)	(b)	(c)	(d)
$a$ [m]	$6.9 \times 10^{-9}$	$1.30 \times 10^{-8}$	$8.53 \times 10^{-9}$	$3.14 \times 10^{-9}$

by  $a$  to compare  $\tau$  with the experimental stresses. By including  $\beta$ ,  $a$ , and  $k_B T$  in the calculation formula of  $\tau$ , we have

$$\begin{aligned} \tau_{\text{sim}} &= \frac{2\gamma \langle S_1 \rangle - 3N + 2N_2 k_B T}{2A_p a^3} \\ &= (4 \times 10^{-21}/a^3)\tau, \end{aligned} \quad (18)$$

where the room temperature is assumed for  $T$ . Note that the simulation data  $\tau$  in Eq. (12) is obtained from this  $\tau_{\text{sim}}$  by assuming  $k_B T = 1$  and  $a = 1$ . Note also that the unit of  $(4 \times 10^{-21}/a^3)$  is  $[\text{m}^{-1}]$  because the units of  $\tau_{\text{sim}}$  and  $\tau$  are given by  $[\text{N}/\text{m}^2]$  and  $[\text{N}/\text{m}]$ , respectively. This  $\tau_{\text{sim}}[\text{N}/\text{m}^2]$  can be identified with experimental stresses if the value of  $a$  is specified. The question is, how can we obtain the coefficient  $(4 \times 10^{-21}/a^3)$  from experimental and simulation data? One possible answer is to determine  $(4 \times 10^{-21}/a^3)$  such that the slope of  $\tau_{\text{sim}}$  equals to that of the experimental data in their linear regions. The slope of  $\tau$  with respect to the strain is just Young modulus  $E_{\text{sim}}$ . Therefore, the experimental and simulation Young moduli  $E_{\text{exp}}$  and  $E_{\text{sim}}$  can be obtained from their linear part of the corresponding experimental nominal stress and  $\tau$  such that the following condition is satisfied:

$$E_{\text{exp.}} = (4 \times 10^{-21}/a^3)E_{\text{sim.}} \quad (19)$$

From this relation, the coefficient  $(4 \times 10^{-21}/a^3)$  is obtained and used to plot  $\tau_{\text{sim}}$  in Figs. 10(a)–10(d). We find in the experimental data that the linear behavior terminates for the large strain region [see Fig. 10(d)]. In contrast, the simulation data  $\tau_{\text{sim}}$  behave only linearly for the large strain region because no failure mechanism is implemented in the model.

From the coefficients  $(4 \times 10^{-21}/a^3)$ , which are obtained from the experimental and simulation data and used for the plots in Figs. 10(a)–10(d), the parameters  $a$  can be obtained and are shown in Table I. The parameters  $a$  are approximately ten times (or more) greater than the van der Waals radius of atoms, and therefore these  $a$  are meaningful as the lattice spacing for the calculations of  $\tau_{\text{sim}}$ .

## IV. SUMMARY AND CONCLUSION

We have studied the origin of the J-shaped stress-strain diagram using Monte Carlo simulations on triangulated surfaces. For such a nonlinear behavior of the J-shaped diagram, it has been widely accepted that the collagen structure plays an essential role [12–17, 19, 20]. However, for the J-shaped diagram, no concrete result has yet been obtained in theoretical or computational evaluations of the curve from the perspective of two-dimensional surface models because the interaction between the collagen and the bulk material (including collagen itself) is too complex.



To understand the mechanism of the J-shaped diagram, we first calculate the frame tension  $\tau$  of cylindrical surfaces using the canonical surface model of HP [38,43,44]. From the Monte Carlo data of the HP model, we find that  $\tau$  is J-shaped. However, the J-shaped curve can be obtained only for some limiting cases, such as small and large bending rigidity  $\kappa$  regions. In fact, for the region of  $\kappa \simeq 1.5$ ,  $\tau$  changes linearly with respect to  $H/H_0$ , including the smaller region  $H/H_0 \simeq 1$ . For this reason, we apply the FG model to evaluate  $\tau$  on the same cylindrical surfaces. The FG model is an extension of the HP model and includes a new degree of freedom  $\sigma$  corresponding to the polymer (or liquid-crystal) direction [27,28,36]. The Monte Carlo results of the FG model for all values of  $\kappa$  are in good agreement with the existing J-shaped stress-strain curves obtained experimentally. This result implies that the J-shaped diagram can be understood in the context of the FG modeling.

The important point to note is that a structural change is essential for the J-shaped curve. This structural change is associated with the directional degrees of freedom of  $\sigma$ , which has two different phases, such as ordered and disordered. A phase transition between these two phases, from the disordered phase to the ordered phase, is activated by an external force that expands the surface. In this expansion process, the external force changes the internal structure represented by  $\sigma$  in the small  $H/H_0$  region. As a result of this structural change, the surface fluctuation property is altered such that a long-range correlation, expected for a certain region of  $\kappa$  in the canonical model, is suppressed due to the one-dimensional correlation of  $\sigma$ . Thus, the internal structural change during the process of surface expansion is the origin of the J-shaped stress-strain diagram of membranes, and this intuitive picture for the interaction between  $\sigma$  and the bulk polymer can be implemented in the FG surface model. We should note that the detailed information on the transition property of this internal structure and the dependence of the J-shaped curve on the internal phase transition remain to be studied.

#### ACKNOWLEDGMENTS

H.K. acknowledges Giancarlo Jug and Andrei Maximov for discussions and comments. The authors acknowledge Eisuke Toyoda for computer analyses. This work is supported in part by JSPS KAKENHI Grants No. 26390138 and No. 17K05149.

#### APPENDIX: FINSLER GEOMETRY MODEL FOR 2D MEMBRANE

We start with the continuous Hamiltonian  $S$ , which is given by

$$\begin{aligned} S &= \gamma S_1 + \kappa S_2, \\ S_1 &= \int \sqrt{g} d^2x g^{ab} \frac{\partial \mathbf{r}}{\partial x_a} \cdot \frac{\partial \mathbf{r}}{\partial x_a}, \\ S_2 &= \frac{1}{2} \int \sqrt{g} d^2x g^{ab} \frac{\partial \mathbf{n}}{\partial x_a} \cdot \frac{\partial \mathbf{n}}{\partial x_b}, \end{aligned} \quad (\text{A1})$$

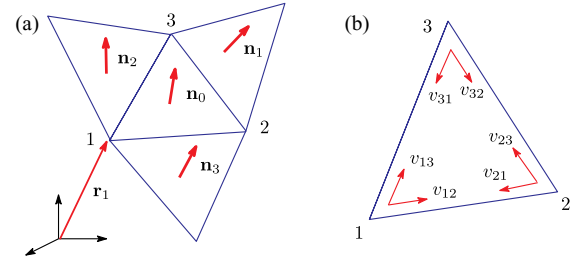


FIG. 11. (a) Tangential component  $v_{ij}$  of  $\sigma_i$  along the direction  $\mathbf{t}_{ij}$  on the triangle 123; (b) the triangle 123 and the three neighboring triangles with unit normal vectors  $\mathbf{n}_i$  ( $i = 0, 1, 2, 3$ );  $\mathbf{r}_1$  is the position of vertex 1.

where  $S_1$  and  $S_2$  are the Gaussian energy and the bending energy, respectively. The coefficients  $\gamma (=1)$  and  $\kappa [1/k_B T]$  are the surface tension and the bending rigidity, respectively, where  $k_B$  and  $T$  are the Boltzmann constant and the temperature. In  $S_1$ ,  $\mathbf{r} (\in \mathbf{R}^3)$  is the surface position [see Fig. 2(b)], which is locally parametrized by  $(x_1, x_2)$ ; hence,  $\mathbf{r}$  is understood to be a mapping from the two-dimensional parameter space  $M$  to  $\mathbf{R}^3$  such that  $M \ni (x_1, x_2) \mapsto \mathbf{r}(x_1, x_2) \in \mathbf{R}^3$ . The  $2 \times 2$  matrix  $g_{ab}$  is a metric function on  $M$ ,  $g^{ab}$  is its inverse, and  $g$  is the determinant of  $g_{ab}$ . The symbol  $\mathbf{n}$  in  $S_2$  is a unit normal vector of the surface  $\mathbf{r}(x_1, x_2)$  in  $\mathbf{R}^3$  (see Ref. [27] for more details). The FG is considered to be a framework for anisotropic phenomena [45–48]. We also note that the J-shaped diagram is expected to share the same origin with the soft elasticity in 3D liquid-crystal elastomers [32–35].

Let  $\sigma_i (\in S^2 : \text{unit sphere})$  be the variable corresponding to the directional degrees of freedom of a polymer or molecule such as liquid crystals at the vertex  $i$  of the triangulated surface. Let  $\mathbf{t}_{ij}$  be the unit tangential vector of the triangle edge (or bond)  $ij$ , which connects the vertices  $i$  and  $j$ , such that  $\mathbf{t}_{ij} = (\mathbf{r}_j - \mathbf{r}_i) / |\mathbf{r}_j - \mathbf{r}_i|$ . Using this  $\mathbf{t}_{ij}$ , we define the tangential component of  $\sigma_i$  along the bond  $ij$  by

$$v_{ij} = |\sigma_i \cdot \mathbf{t}_{ij}|. \quad (\text{A2})$$

We note that  $v_{ij} \neq v_{ji}$  in general.

Let 123 denote a triangle on  $M$ , and let the vertex 1 be the local coordinate origin of the triangle 123 (Fig. 11); then, the Finsler metric  $g_{ab}$  on the triangle 123 is defined by

$$g_{ab} = \begin{pmatrix} 1/v_{12}^2 & 0 \\ 0 & 1/v_{13}^2 \end{pmatrix}. \quad (\text{A3})$$

Thus, by the replacements

$$\begin{aligned} \partial_1 \mathbf{r} &\rightarrow \mathbf{r}_2 - \mathbf{r}_1, & \partial_2 \mathbf{r} &\rightarrow \mathbf{r}_3 - \mathbf{r}_1, \\ \partial_1 \mathbf{n} &\rightarrow \mathbf{n}_0 - \mathbf{n}_2, & \partial_2 \mathbf{n} &\rightarrow \mathbf{n}_0 - \mathbf{n}_3, \end{aligned}$$

$$\int \sqrt{g} d^2x \rightarrow \frac{1}{2} \sum_{\Delta} \sqrt{\det g_{ab}} \quad (\text{A4})$$

in Eq. (A1), we have

$$\begin{aligned} S_1 &= \frac{1}{2} \sum_{\Delta} \left[ \frac{v_{12}}{v_{13}} \ell_{12}^2 + \frac{v_{13}}{v_{12}} \ell_{13}^2 \right], & \ell_{ij}^2 &= (\mathbf{r}_i - \mathbf{r}_j)^2, \\ S_2 &= \frac{1}{2} \sum_{\Delta} \left[ \frac{v_{13}}{v_{12}} (1 - \mathbf{n}_0 \cdot \mathbf{n}_3) + \frac{v_{12}}{v_{13}} (1 - \mathbf{n}_0 \cdot \mathbf{n}_2) \right]. \end{aligned} \quad (\text{A5})$$

Because there are three possible local coordinate origins on the triangle 123, all possible terms in  $S_1$  and  $S_2$  should be summed over with the coefficient  $1/3$ . The sum over triangles  $\sum_{\Delta}$  in both  $S_1$  and  $S_2$  can be replaced by the sum over bonds  $\sum_{ij}$ ; then, we finally obtain

$$S_1 = \frac{1}{6} \sum_{\Delta} [\gamma_{12} \ell_{12}^2 + \gamma_{23} \ell_{23}^2 + \gamma_{31} \ell_{31}^2],$$

$$S_2 = \frac{1}{6} \sum_{\Delta} [\kappa_{12}(1 - \mathbf{n}_0 \cdot \mathbf{n}_3) + \kappa_{23}(1 - \mathbf{n}_0 \cdot \mathbf{n}_1) + \kappa_{31}(1 - \mathbf{n}_0 \cdot \mathbf{n}_2)],$$

$$\gamma_{12} = \frac{v_{12}}{v_{13}} + \frac{v_{21}}{v_{23}}, \quad \gamma_{23} = \frac{v_{23}}{v_{21}} + \frac{v_{32}}{v_{31}},$$

$$\gamma_{31} = \frac{v_{31}}{v_{32}} + \frac{v_{13}}{v_{12}},$$

$$\kappa_{12} = \frac{v_{13}}{v_{12}} + \frac{v_{23}}{v_{21}}, \quad \kappa_{23} = \frac{v_{21}}{v_{23}} + \frac{v_{31}}{v_{32}},$$

$$\kappa_{31} = \frac{v_{32}}{v_{31}} + \frac{v_{12}}{v_{13}}. \quad (\text{A6})$$

Multiplying  $\gamma(=1)$  by  $\gamma_{ij}$  and  $\kappa$  by  $\kappa_{ij}$ , we have  $\gamma\gamma_{ij}$  and  $\kappa\kappa_{ij}$ , which can be considered to be effective surface tension and effective bending rigidity. These quantities  $\gamma\gamma_{ij}$  and  $\kappa\kappa_{ij}$  are dependent on the position and the direction of the bond  $ij$ , although  $\gamma_{ij}$  and  $\kappa_{ij}$  are a part of energies  $S_1$  and  $S_2$ , respectively. This dependence of  $\gamma_{ij}$  and  $\kappa_{ij}$  on the position and the direction of the bond is the most interesting output of the FG model. Anisotropic coefficients are expected to play an important role for the anisotropy in LCE [49–52]. Note that both  $S_1$  and  $S_2$  are explicitly dependent on  $\sigma$  because  $\gamma_{ij}$  and  $\kappa_{ij}$  are determined by  $\sigma$  via Eq. (A2).

- 
- [1] J. P. Chowa, D. T. Simionescu, H. Warner, B. Wang, S. S. Patnaik, J. Liao, and A. Simionescu, *Biomaterials* **34**, 685 (2013).
- [2] M. A. Meyers, P. Chen, A. Y. Lin, and Y. Seki, *Prog. Mater. Sci.* **53**, 1 (2008).
- [3] H. Greven, K. Zanger, and G. Schwinger, *J. Morphology* **224**, 15 (1995).
- [4] P. Fratzl, K. Misof, I. Zizak, G. Rapp, H. Amenitsch, and S. Bernstorff, *J. Struct. Biol.* **122**, 119 (1997).
- [5] G. Tronci, A. Doyle, S. J. Russell, and D. J. Wood, *J. Mater. Chem. B* **1**, 5478 (2013).
- [6] A. E. Toscano, K. M. Ferraz, R. M. de Castro, and F. Canon, *Clinics* **65**, 1363 (2010).
- [7] K. Kokini, J. E. Sturgis, J. P. Robinson, and S. L. Voytik-Harbin, *J. Biomech. Eng.* **124**, 214 (2002).
- [8] D. Seliktar, R. A. Black, R. P. Vito, and R. M. Nerem, *Ann. Biomed. Eng.* **28**, 351 (2000).
- [9] P. J. Flory, *Principles of Polymer Chemistry* (Cornell University, Ithaca, 1953).
- [10] B. Xua, Y. Lia, X. Fanga, G. A. Thouasb, W. D. Cooka, D. F. Newgreenc, and Q. Chena, *J. Mech. Behav. Biomed. Mater.* **28**, 354 (2013).
- [11] A. Gautieri, S. Vesentini, A. Redaelli, and M. J. Buehler, *Nano Lett.* **11**, 757 (2011).
- [12] W. Maier and A. Saupe, *Zeitschrift für Naturforschung A* **13A**, 564 (1958); **14A**, 882 (1959); **15A**, 287 (1960).
- [13] P.-G. de Gennes, *Scaling Concepts in Polymer Physics* (Cornell University Press, Ithaca, 1979).
- [14] M. Doi and S. F. Edwards, *The Theory of Polymer Dynamics* (Oxford University Press, New York, 1986).
- [15] A. Levillain, M. Orhant, F. Turquier, and T. Hoc, *J. Mech. Behav. Biomed. Mater.* **61**, 308 (2016).
- [16] E. M. Huisman, C. Storm, and G. T. Barkema, *Phys. Rev. E* **78**, 051801 (2008).
- [17] D. A. Head, A. J. Levine, and F. C. MacKintosh, *Phys. Rev. E* **68**, 061907 (2003).
- [18] G. Jug, M. Paliienko, and S. Bonfanti, *J. Non-Cryst. Solids* **401**, 66 (2014).
- [19] S. Pradhan, A. Hansen, and B. K. Chakrabarti, *Rev. Mod. Phys.* **82**, 499 (2010).
- [20] T. Giesa, N. M. Pugno, and M. J. Buehler, *Phys. Rev. E* **86**, 041902 (2012).
- [21] W. Helfrich, *Zeitschrift für Naturforschung A* **28c**, 693 (1973).
- [22] A. M. Polyakov, *Nucl. Phys. B* **268**, 406 (1986).
- [23] M. Bowick and A. Travasset, *Phys. Rep.* **344**, 255 (2001).
- [24] K. J. Wiese, in *Phase Transitions and Critical Phenomena*, edited by C. Domb and J. L. Lebowitz (Academic, New York, 2000), Vol. 19, p. 253.
- [25] D. Nelson, in *Statistical Mechanics of Membranes and Surfaces*, 2nd ed., edited by D. Nelson, T. Piran, and S. Weinberg (World Scientific, Singapore, 2004), p. 1.
- [26] G. Gompper and D. M. Kroll, Triangulated-surface models of fluctuating membranes, in *Statistical Mechanics of Membranes and Surfaces*, 2nd ed., edited by D. Nelson, T. Piran, and S. Weinberg (World Scientific, Singapore, 2004), p. 359.
- [27] H. Koibuchi and H. Sekino, *Physica A* **393**, 37 (2014).
- [28] K. Osari and H. Koibuchi, *Polymer* **114**, 355 (2017).
- [29] J. F. Wheeler, *J. Phys. A: Math. Gen.* **27**, 3323 (1994).
- [30] W. Cai, T. C. Lubensky, P. Nelson, and T. Powers, *J. Phys. II (France)* **4**, 931 (1994).
- [31] F. David and S. Leibler, *J. Phys. II (France)* **1**, 959 (1991).
- [32] M. Wamer and E. M. Terentjev, *Liquid Crystal Elastomer* (Oxford University Press, New York, 2007).
- [33] V. Domenici, *Prog. Nucl. Magn. Reson. Spectrosc.* **63**, 1 (2012).
- [34] E. M. Terentjev, *J. Phys.: Condens. Matter* **11**, R239 (1999).
- [35] I. Kundler and H. Finkelmann, *Macromol. Chem. Phys.* **199**, 677 (1998).
- [36] H. Koibuchi and A. Shobukhov, *Int. J. Mod. Phys. C* **27**, 1650042 (2016); **27**, 1692001(E) (2016).
- [37] P. A. Lewohl and G. Lasher, *Phys. Rev. A* **6**, 426 (1972).
- [38] H. Koibuchi, A. Shobukhov, and H. Sekino, *J. Math. Chem.* **54**, 358 (2016).
- [39] N. Metropolis, A. W. Rosenbluth, M. N. Rosenbluth, and A. H. Teller, *J. Chem. Phys.* **21**, 1087 (1953).
- [40] D. P. Landau, *Phys. Rev. B* **13**, 2997 (1976).
- [41] H. Koibuchi, *Phys. Rev. E* **77**, 021104 (2008).
- [42] M. Creutz, *Quarks, Gluons and Lattices* (Cambridge University Press, Cambridge, 1983).
- [43] M. J. Bowick, A. Cacciuto, G. Thorleifsson, and A. Travasset, *Eur. Phys. J. E* **5**, 149 (2001).

- [44] R. Cuerno, R. Gallardo Caballero, A. Gordillo-Guerrero, P. Monroy, and J. J. Ruiz-Lorenzo, *Phys. Rev. E* **93**, 022111 (2016).
- [45] M. Matsumoto, *Keiryō Bibun Kikagaku* (in Japanese) (Shokabo, Tokyo, 1975).
- [46] D. Bao, S.-S. Chern, and Z. Shen, *An Introduction to Riemann-Finsler Geometry* (Springer, New York, 2000).
- [47] G. Bogoslovsky, *Int. J. Geom. Methods Mod. Phys.* **9**, 1250007 (2012).
- [48] G. Bogoslovsky, *Phys. Lett. A* **244**, 222 (1998).
- [49] T. C. Lubensky, R. Mukhopadhyay, L. Radzihovsky, and X. Xing, *Phys. Rev. E* **66**, 011702 (2002).
- [50] X. Xing, R. Mukhopadhyay, T. C. Lubensky, and L. Radzihovsky, *Phys. Rev. E* **68**, 021108 (2003).
- [51] X. Xing and L. Radzihovsky, *Ann. Phys. (NY)* **323**, 105 (2008).
- [52] O. Stenull and T. C. Lubensky, *Phys. Rev. Lett.* **94**, 018304 (2005).